Physics and Chemistry of Minerals
https://doi.org/10.1007/s00269-019-01056-8

ORIGINAL PAPER

Compressional behavior of end-member and aluminous iron-bearing diopside at high pressure from single-crystal X-ray diffraction and first principles calculations

Yi Hu[1] · Boris Kiefer[2] · Anna Plonka[3] · John B. Parise[4] · Jin S. Zhang[5] · Murli H. Manghnani[6] · Baikuntha N. Sahu[7] · Przemyslaw K. Dera[6]

Received: 31 January 2019 / Accepted: 27 September 2019

Abstract

Diopside ($CaMgSi_2O_6$), the Ca- and Mg-rich clinopyroxene is an important mineral in the Earth's upper mantle and subducted lithospheric plate. Here, we report the results of high-pressure single-crystal X-ray diffraction experiments conducted on a natural aluminous iron-bearing diopside and a natural, nearly end-member diopside, up to 50 GPa in diamond anvil cell. Density functional theory calculation results on end-member diopside are also reported. Unit cell parameters a, b, c, β, V, as well as bond lengths of diopside are reported and compared with other clinopyroxenes. Bulk modulus and its pressure derivative of the two diopside samples are determined using third-order Birch–Murnaghan equation of state. The density of the two diopside samples is calculated under cold subducting slab conditions and is compared with the seismic models. Along the cold slab geotherm, aluminous iron-bearing diopside has higher density than end-member diopside. In the upper mantle, eclogite with aluminous iron-bearing diopside is denser than eclogite with end-member diopside, and, therefore, provides larger slab pulling force. At the bottom of the transition zone and the top of the lower mantle, eclogite with aluminous iron-bearing diopside, though higher in density than the end-member diopside, is still less dense than the surrounding mantle and could contribute to the slab stagnation.

Keywords Diopside · Pyroxene · High pressure · Equation of state

Introduction

Diopside ($CaMgSi_2O_6$), the Ca- and Mg-rich clinopyroxene (cpx) is an important mineral in the Earth's upper mantle. In the pyrolite and piclogite upper mantle models, clinopyroxene constitutes about 15% and 35%, respectively, of the total minerals in the top portion of the upper mantle (Ringwood 1975; Frost 2008; Ita and Stixrude 1992; Anderson and Bass 1984; Bass and Anderson 1984). As depth increases, clinopyroxene gradually dissolves into garnet and forms majorite at the depth of transition zone (Ringwood 1967).

Diopside is also an important mineral in the subducting slab. Eclogite—a rock formed by high-pressure metamorphism of basalt or gabbro at subduction zones—is mainly composed of clinopyroxene (60–70 vol%) and garnet (20–30 vol%) (Ringwood 1982; Poli 1993), though the pyroxene is typically enriched in Na and Al, and classified as omphacite. When temperature is sufficiently high (e.g., >1300 K), omphacite slowly dissolves into garnet at depths greater than 300 km, transforming eclogite into garnetite

---

Electronic supplementary material The online version of this article (https://doi.org/10.1007/s00269-019-01056-8) contains supplementary material, which is available to authorized users.

✉ Przemyslaw K. Dera
pdera@hawaii.edu

[1] Department of Geology and Geophysics, University of Hawaii at Manoa, Honolulu, HI, USA

[2] Department of Physics, New Mexico State University, Las Cruces, NM, USA

[3] Department of Materials Science and Chemical Engineering, Stony Brook University, Stony Brook, NY, USA

[4] Department of Geosciences, Stony Brook University, Stony Brook, NY, USA

[5] Department of Earth and Planetary Sciences, Institute of Meteoritics, University of New Mexico, Albuquerque, NM, USA

[6] Hawaii Institute of Geophysics and Planetology, University of Hawaii at Manoa, Honolulu, HI, USA

[7] Department of Physics and Astronomy, National Institute of Technology, Rourkela, Odisha, India

(Ringwood 1982). This transition is highly dependent on temperature profile of the subducting slab, which varies with the age of the sea floor. Recent studies show that at temperatures well below the mantle geotherm, pyroxene-garnet transformation is kinetically inhibited at the conditions of the subducting slab, so that clinopyroxene may be well preserved down to the transition zone, or even the top of the lower mantle in the subducting slab (Nishi et al. 2008, 2013; Van Mierlo et al. 2013).

Seismic studies show a large variety of subducting slab morphologies near the base of the mantle transition zone, between 400 and 800 km depth. Some subducted slabs sink into the lower mantle, for example, beneath the Central America, while others seem to flatten and stagnate, for example, beneath the Izu–Bonin region (Fukao et al. 2009; Fukao and Obayashi 2013). Another notable phenomenon is that hot (>1200 K) slabs are dominated by absence of stagnation, while cold (<1200 K) slabs are dominated by stagnation (King et al. 2015). The preservation of metastable clinopyroxenes at the transition zone provides a good explanation to the cold stagnant slab phenomenon—cold environment preserves the metastable phases which are less dense than the surrounding stable phases, thus providing buoyancy force to the slab. As a consequence, the metastability and density of pyroxene below 1200 K play an important role in slab dynamics (Faccenda and Dal Zilio 2017; Nishi et al. 2011; Van Mierlo et al. 2013).

Pyroxenes are also found in various meteorites, including ordinary and carbonaceous chondrites, as well as in the silicate inclusions in iron meteorites (Rubin 1997). Some studies report the observation of diopside in heavily shocked chondrites (Rubin 1997; Zhang et al. 2006; Tomioka and Kimura 2003), which suggests that it can survive to pressure beyond the established stable region. Therefore, the study of diopside at high pressure is also important to explain its behavior in the shock process (Svendsen and Ahrens 1983, 1990; Rigden et al. 1989).

Clinopyroxenes, with a general formula $M2M1(Si, Al)_2O_6$ and a C2/c space group at ambient conditions, have crystal structures consisting of alternating layers of tetrahedral chains and layers of octahedrally coordinated cations. The flexibility of the tetrahedra to rotate with respect to one another allows the structure to accommodate cations with different ionic radii, leading to a wide range of possible compositions (Cameron and Papike 1981). In this structure, M2 is usually occupied by large cations such as Ca^{2+}, Na^{+}, Mn^{2+}, Fe^{2+}, Mg^{2+}, and Li^{+}, whereas M1 is usually occupied by smaller cations such as Mn^{2+}, Fe^{2+}, Mg^{2+}, Fe^{3+}, Al^{3+}, and Ti^{4+}. The subducted oceanic crust is rich in Fe^{2+} and Al^{3+} (Ringwood 1982). The down-going sediments carried by the crust also contain Fe- and Al-rich pelitic packages (Plank and Langmuir 1998; Poli and Schmidt 2002). Thus, it is likely that Fe^{2+} and Al^{3+} are present in the subducted pyroxene. The presence of Fe^{2+} and Al^{3+} in pyroxene structure has been known to affect the density. Hedenbergite ($CaFeSi_2O_6$), the Ca- and Fe-end-member clinopyroxene, has ~12% higher density than diopside (Zhang et al. 1997), while Ca-Tschermak ($CaAl_2SiO_6$), the Ca- and Al-end-member clinopyroxene, has ~5% lower density than diopside (Flemming et al. 2015).

Diopside has been the subject of several high-pressure studies. The equation of state of diopside has been well determined to ~15 GPa (Zhang et al. 1997; Zhao 1998; Li and Neuville 2010; Sang and Bass 2014; Thompson and Downs 2008) by single-crystal or powder X-ray diffraction. Diopside is thermodynamically stable to ~17 GPa. Above 17 GPa and 1400 °C, diopside decomposes into a mixture of product phases including Mg-rich $(Mg, Ca)SiO_3$ garnet and $CaSiO_3$-rich perovskite (Akaogi et al. 2004; Canil 1994). Below 1400 °C, diopside dissociates to Ca–perovskite, wadsleyite, and stishovite (Kim et al. 1994; Oguri et al. 1997). Above 20 GPa, between 1000 and 1900 °C, diopside is observed to break down to Mg–perovskite and Ca–perovskite (Irifune et al. 2000; Liu 1979). At ~1300° and 32 GPa, a metastable cubic CM–perovskite $Ca(Mg, Fe, Al)Si_2O_6$ phase was observed (Asahara et al. 2005). However, at ambient temperature, where the diffusion is slow, diopside can be preserved to pressures well above its thermodynamically stable region. The structure of diopside was determined up to ~55 GPa on an end-member and an aluminous Fe-bearing diopside (Plonka et al. 2012; Hu et al. 2017). Two new high-pressure phases, one featuring 4- and 6-coordinated Si and one featuring rare 5- and 6-coordinated Si, were observed (Plonka et al. 2012; Hu et al. 2017). In this study, we conducted high-pressure single-crystal X-ray diffraction experiments on end-member diopside and aluminous Fe-bearing diopside. We studied the equation of state of diopside and also the compositional effects on volume.

Methods

Two samples were used in the experiments: (1) nearly end-member diopside $Ca(Mg_{0.97}Fe_{0.03})(Al_{0.01}Si_{1.99})O_6$ (denoted as Di_Mg_{97} below) and (2) aluminous Fe-bearing diopside $(Ca_{0.858}Fe^{2+}_{0.098}Na_{0.030}Mn_{0.006}K_{0.003})(Mg_{0.752}Fe^{2+}_{0.153}Al_{0.064}Fe^{3+}_{0.020}Ti_{0.011})(Si_{1.936}Al_{0.064})O_6$ (denoted as Di_Mg_{75} below). Di_Mg_{97} is the same sample used in Plonka et al. (2012) and Di_Mg_{75} the same sample used in Hu et al. (2017), Di_Mg_{75} is a natural sample from the Harry Hess collection at Princeton University (designated as sample C' in Subramanian (1962)).

High-pressure experiments were performed at the synchrotron beamline 13ID-D of the Advanced Photon Source at Argonne National Laboratory. One Di_Mg_{97} crystal was loaded into a symmetric piston-cylinder Princeton-type diamond anvil cell (DAC) with a total opening of 54°. Neon pressure medium was loaded using the GSECARS/COMPRES gas-loading system (Rivers et al. 2008). One Di_Mg_{75} crystal was loaded in helium pressure medium into a diamond anvil cell equipped with conical diamond anvils, featuring 70° total X-ray opening.

Pressure inside the DACs was determined using ruby fluorescence (Mao et al. 1986) and neon diffraction (Dewaele et al. 2008). Diffraction data were collected with a MAR165 Charge Coupled Device (CCD) detector at incident energy of 37.7 keV, following the same procedure, as described in Dera et al. (2013a). Diffraction images were processed using ATREX software package (Dera et al. 2013b), and the structure refinements were conducted using SHELXL (Sheldrick 2008). The refinement details of the two phases are listed in Table S1 and Table S2. VESTA program was used for calculation of polyhedral geometry parameters (Momma and Izumi 2011). Single-crystal X-ray diffraction data were collected at each pressure point. The principal component analysis was done using the Scikit-learn package (Pedregosa et al. 2011).

Density functional theory (DFT) calculations were performed using the Vienna Ab-initio Simulation Package (VASP) (Kresse and Furthmüller 1996a, b), with the electronic exchange and correlation described using the local-density approximations(LDA) (Perdew and Zunger 1981). The Brillouin zone was sampled on a 2×2×4 Monkhorst-Pack grid and a plane-wave cutoff energy of 700 eV was used. The projector augmented wave method (PAW) was used in describing the interactions between atoms (Blöchl 1994; Kresse and Furthmüller 1996a). The core region cutoff radii of the PAW potentials for Ca, Mg, Si, and O were 3.0 a_B, 2.0 a_B, 1.6 a_B, and 1.52 a_B, respectively (1 a_B = 0.529 Å). These computational settings are similar to the previous works on pyroxene (Walker et al. 2008; Walker 2012). The DFT calculations were performed in C2/c space group and all athermal structural optimizations were performed at constant volume. All crystallographic degrees of freedom consistent with the crystal symmetry were relaxed simultaneously until deviatoric stresses were less than 0.05 GPa. The calculations were performed under static conditions. Zero-point vibrations and thermal vibrations were not considered.

Results and discussion

Equation of state

The volume changes of different clinopyroxenes with pressure up to 50 GPa are plotted in Fig. 1a and a detailed comparison with existing data up to 15 GPa is shown in Fig. 1b. The volumes of diopside determined in this study show good agreement with those from literature in the low-pressure regime (Zhang et al. 1997; Zhao 1998; Thompson and Downs 2008; Li and Neuville 2010; Sang and Bass 2014). The differences between Di_Mg_{75}, Di_Mg_{97}, and $Di_{80}En_{20}$ become more pronounced at high pressure, as shown in Fig. 1a, which is most likely due to the compositional effect. The ambient volumes of end-member diopside ($CaMgSi_2O_6$), hedenbergite ($CaFeSi_2O_6$) and Ca-Tschermak ($CaAlAlSiO_6$) are 438.82(11), 449.90(7) and 421.86(2) Å^3, respectively (Zhang et al. 1997; Flemming et al. 2015). The volume of diopside is ~ 2.5% smaller than hedenbergite, and is ~ 4.0% larger than Ca-Tschermak, which indicates that iron increases the volume, while aluminum decreases the volume in Ca-rich clinopyroxenes.

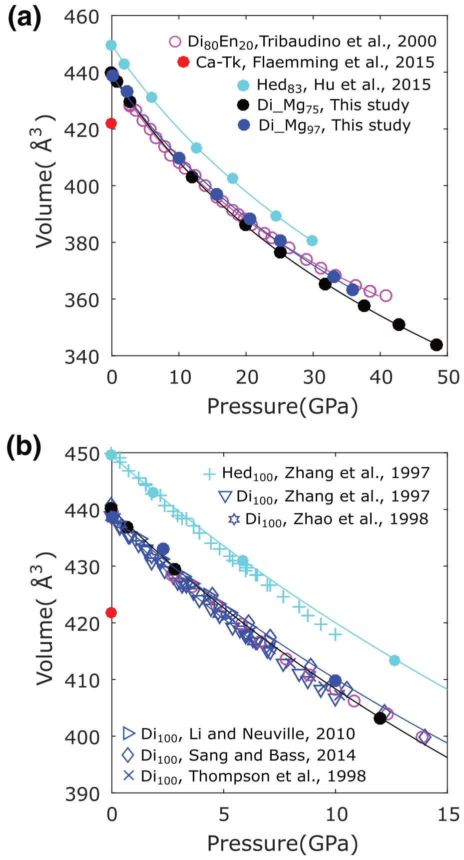

Fig. 1 **a** Pressure–volume relationship and the equation of state fit of different clinopyroxenes up to ~ 50 GPa. **b** Pressure–volume relationship and the equation of state fit of different clinopyroxenes up to 15 GPa

The bulk modulus (K_{T0}) and its pressure derivative (K_{T0}') can be determined from a weighted nonlinear least-squares fitting of 3rd-order Birch–Murnaghan equation of state (BM3) Eq. 1:

$$P(V) = \frac{3K_{T0}}{2}\left[\left(\frac{V_0}{V}\right)^{7/3} - \left(\frac{V_0}{V}\right)^{5/3}\right] \times \left\{1 + \frac{3}{4}(K'_{T0} - 4)\left[\left(\frac{V_0}{V}\right)^{2/3} - 1\right]\right\} \quad (1)$$

where P is pressure, V and V_0 represent the volumes at high and ambient pressure (Hazen and Downs 2000), $\frac{1}{\sigma(V)^2}$ is used as the weighting factor ($\sigma(V)$ is the uncertainty of volume from the experiments) and V_0 is constrained by the ambient measurement. The unit-cell volume of *Di_Mg*$_{97}$ is determined as 438.75(3) Å^3 by single-crystal X-ray diffraction. The bulk modulus and its pressure derivative of *Di_Mg*$_{97}$ are determined as 129(3) GPa and 4.2(3) from BM3 fitting. The BM3 fitting results of *Di_Mg*$_{97}$ yield K_{T0} = 124(3) GPa and K_{T0}' = 4.4(3). The BM3 fitting of DFT calculated volumes on end-member diopside yields K_{T0} = 128(4) GPa and K_{T0}' = 4.0(2), which shows a comparable bulk modulus with *Di_Mg*$_{97}$. The discrepancies between experimental and DFT results are mainly from the neglect of thermal vibrations (temperature effect) and zero-point vibrations in the calculations. The bulk modulus and its pressure derivative of *Di_Mg*$_{75}$ determined from fitting BM3 are 113(1) GPa and 4.46(9), respectively. Based on those results, we conclude that Fe and Al in diopside structure decrease the bulk modulus.

Figure S1 shows the F_E-f_E plot of both diopside samples, depicting a relationship between Eulerian strain f_E (Eq. 3) and Birch normalized stress F_E (Eq. 4):

$$F_E = K_{T0}[1 + 1.5f_E(K'_{T0} - 4)] \quad (2)$$

where

$$f_E = [(V/V_0)^{-2/3} - 1]/2 \quad (3)$$

and

$$F_E = P/[3f_E(1 + 2f_E)^{5/2}] \quad (4)$$

In this fitting, $\frac{1}{\sigma(V)^2}$ is used as the weighting factor. The K_{T0} = 112(1) GPa and K'_{T0} = 4.5(1) of *Di_Mg*$_{75}$ obtained from linear f_E–F_E fit are in good agreement with the values from direct BM3 fitting (K_{T0} = 113(1) GPa and K'_{T0} = 4.46(9)). The K_{T0} and K'_{T0} of *Di_Mg*$_{97}$ from f_E-F_E plot are determined to be 127(3) GPa and 4.3(3), and also agree well with the values from BM3 fitting.

The K_{T0} and K'_{T0} confidence ellipses of different kinds of clinopyroxenes (with a confidence level of ± 68.3%) are plotted together with *Di_Mg*$_{75}$ and *Di_Mg*$_{97}$ in Fig. 2. The

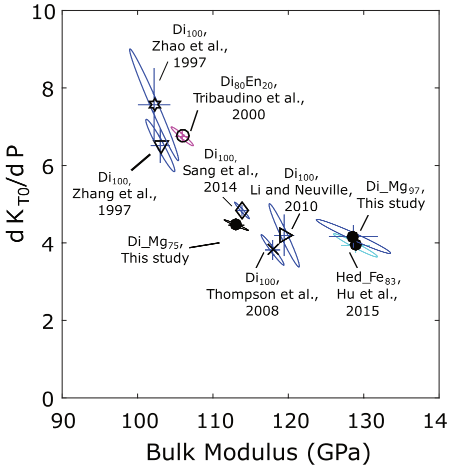

Fig. 2 K_{T0} and K_{T0}' ellipses with a confidence level of ± 68.3% of different clinopyroxene compositions

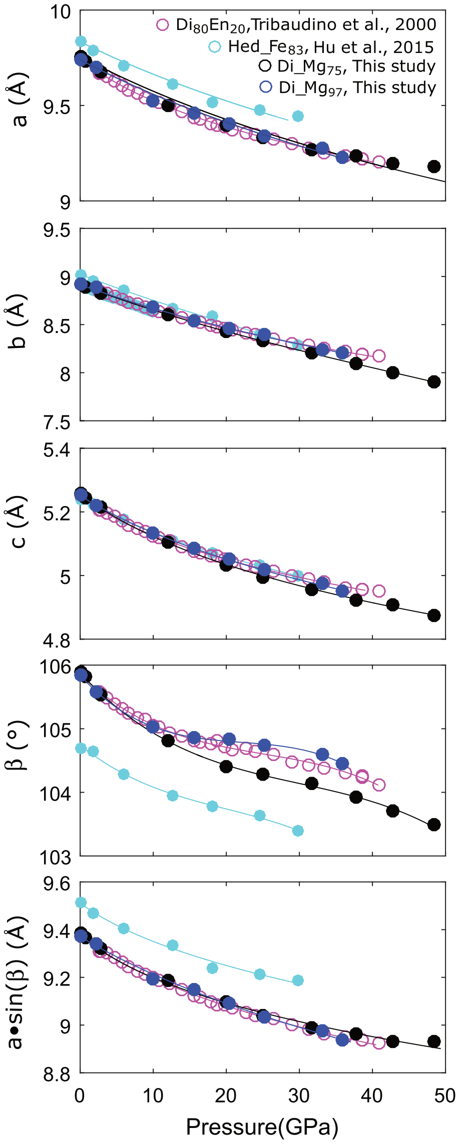

Fig. 3 Unit cell parameters of clinopyroxenes at high pressure

K_{T0} and K'_{T0} of *Di_Mg*$_{75}$ and *Di_Mg*$_{97}$ determined from fitting BM3 are similar to the observations in Sang and Bass (2014); Li and Neuville (2010); Thompson and Downs (2008) (the K_{T0} and K'_{T0} from other papers are recalculated from the reported unit cell volumes), but are different from the values determined by Zhao (1998) and Zhang et al. (1997). The discrepancy between the data is probably due to pressure calibration. Hedenbergite shows larger K_{T0} than diopside (Hu et al. 2015) and aluminous iron-bearing diopside has smaller K_{T0} than nearly end-member diopside. This indicates that Fe in diopside structure tends to increase bulk modulus and Al in diopside structure tends to decreases bulk modulus. However, the variation with changes in composition is weak, which is consistent with the observation in Kandelin and Weidner (1988).

Structure comparison

The unit cell parameters of both diopside samples along with *Hed_Fe*$_{83}$ (Hu et al. 2015) at different pressures are shown in Fig. 3 and are tabulated in Tables 1 and 2. Clinopyroxenes can be described as layered structures. The Si–O tetrahedral chains extend along the *c* direction with M1 and M2 cations located between the chains. *a* axis points in the direction perpendicular to the layers, and therefore, the length of *a*-axis is mainly controlled by chemical composition. Both diopside samples have similar value of *a* , which is ~ 0.8% smaller than hedenbergite, and is caused by the small cation size of Mg^{2+}, compared to Fe^{2+}. This effect can also be observed in the average M1–O bond length and $M1O_6$ polyhedral volumes, as shown in Figs. 4a, b. The average bond length of M1–O in hedenbergite is larger than in diopside, and the polyhedral volume of $M1O_6$ in hedenbergite is also larger than in diopside. The *b* unit cell parameter of hedenbergite is ~1.1% greater than that of diopside. The unit cell length along the *c* direction is controlled by O3–O3–O3 angle. The O3–O3–O3 angle is almost the same in diopside and hedenbergite, in the range of ~165°-156°. The values of the *c* lattice parameter of all diopside phases compared here are about the same. The *β* angles of diopside decrease significantly upon compression at relatively low pressure. The Mg-rich samples *Di_Mg*$_{97}$ and $Di_{80}En_{20}$ show a flattening in *β* angle at ~30 GPa. The *β* angle of diopside is ~1.1% higher than that of hedenbergite. Similar analyses are also found in the previous literature (Zhang et al. 1997).

Compositional effect on unit cell volume

Density is an important property of minerals, which is responsible for both the positive and negative buoyancy force of the slab (Hu et al. 2016), and therefore affects the slab dynamics.

Table 1 Unit cell parameters of *Di_Mg*$_{75}$

Exp. No.	Pressure(GPa)	*a*(Å)	*b*(Å)	*c*(Å)	*β*(°)	Volume(Å^3)
P0	0.00001	9.7578(9)	8.9168(9)	5.2584(5)	105.885(9)	440.05(8)
P1	0.7(1)	9.733(1)	8.8930(9)	5.2450(5)	105.809(9)	436.81(8)
P2	2.8(1)	9.676(1)	8.830(1)	5.2164(6)	105.52(1)	429.41(9)
P3	12.0(4)	9.500(1)	8.5954(7)	5.1066(4)	104.815(9)	403.13(7)
P4	19.9(4)	9.394(2)	8.4345(9)	5.0336(5)	104.40(1)	386.32(9)
P5	25.0(4)	9.331(1)	8.3333(9)	4.9960(5)	104.28(1)	376.46(8)
P6	31.7(4)	9.268(1)	8.2008(9)	4.9584(5)	104.14(1)	365.45(8)
P7	37.7(4)	9.238(1)	8.096(1)	4.9242(5)	103.92(1)	357.43(8)
P8	42.7(4)	9.193(2)	8.006(1)	4.9061(7)	103.70(2)	350.8(1)
P9	48.4(4)	9.181(2)	7.897(2)	4.8764(8)	103.48(2)	343.8(1)

Table 2 Unit cell parameters of *Di_Mg*$_{97}$

Exp. No.	Pressure(GPa)	*a*(Å)	*b*(Å)	*c*(Å)	*β*(°)	Volume(Å^3)
P0	0.00001	9.7403(4)	8.9163(4)	5.2514(2)	105.839(1)	438.75(3)
P1	2.28(3)	9.696(9)	8.882(9)	5.220(2)	105.58(3)	433.0(6)
P2	9.99(2)	9.522(4)	8.685(3)	5.1324(6)	105.03(1)	409.9(2)
P3	15.62(3)	9.463(3)	8.533(3)	5.0846(5)	104.85(1)	396.8(2)
P4	20.5(1)	9.406(6)	8.459(5)	5.050(1)	104.83(2)	388.4(3)
P5	25.2(2)	9.340(6)	8.400(5)	5.019(1)	104.73(2)	380.8(3)
P6	33.1(2)	9.273(6)	8.245(5)	4.9738(9)	104.60(2)	368.0(3)
P7	35.9(2)	9.230(3)	8.205(3)	4.9522(6)	104.45(3)	363.2(2)

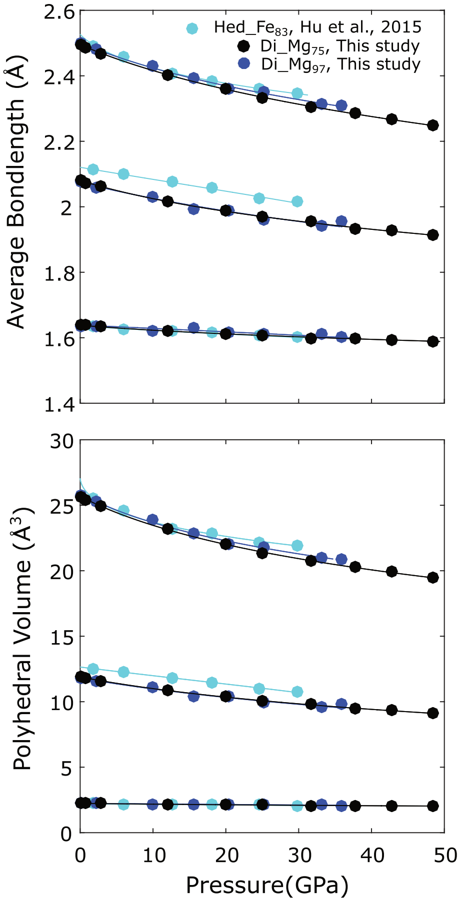

Fig. 4 Polyhedral volumes of clinopyroxenes at high pressure

Modeling of density of minerals with complex compositions is not trivial. The unit cell volumes of such minerals can be estimated through thermodynamic mixing (Green et al. 2007). However, the composition of natural diopside is very complicated and thermodynamic modeling can be challenging and require a lot of data of end-member or simple-composition samples, which are hard to obtain. Therefore, in this study, we used statistical methods instead of physical model to analyze the compositional effect on density. The details of the analysis are described in the supplementary materials. In order to model the relationship between composition and unit cell volume, data from the RRUFF mineral database are analyzed together with data obtained in this study, as shown in Table S3. In this table, columns 2–16 (15 columns in total) show the fraction of atoms of different elements in each crystallographic site multiplied by 100, and the last column shows the unit cell volume. The columns 2–16 are used as the input (old vectors) and are decomposed to four new principal vectors using principal component analysis (PCA), and then multi-dimensional linear regression is used to fit the relation between the four new vectors and the unit cell volume (James et al. 2013).

Principal component analysis is a method allowing to find a low-dimensional representation of the data that has the maximum variation, which is equivalent to finding a set of more combined parameters to which the analyzed function is most sensitive. Each of the new vectors found by PCA is a linear combination of the normalized old vectors. The i^{th} vector in the new space is represented by

$$\mathbf{Z_i} = t_{1i}\mathbf{X_1} + t_{2i}\mathbf{X_2} + \ldots + t_{m_1 i}\mathbf{X_{m_1}}, 0 \le i \le m_2, \tag{5}$$

where $\mathbf{X} = \{\mathbf{X_1}^T;\mathbf{X_2}^T;\ldots;\mathbf{X_{m_1}}^T\}$ (the superscript T means transpose) is the normalized old vector which has dimension $n \times m_1$ (n is the sample size and m_1 is the dimension of the old space). t_{ij} is the element of the transformation matrix $\mathbf{T}$ and m_2 is the dimension of the new space. Therefore, Eq. 5 can be represented as

$$\mathbf{Z} = \mathbf{X} \cdot \mathbf{T}. \tag{6}$$

The matrix $\mathbf{T}$, which maximizes the variation of the new vectors, can be found via eigen decomposition or singular value decomposition. The transformation matrix $\mathbf{T}$ has dimensions $m_1 \times m_2$. Here, we picked 38 clinopyroxene samples, as listed in Table S3. The transformation matrix is listed in the supplementary material (sup_trans_matrix.txt). The four new principal vectors forming the $\mathbf{Z} = \{\mathbf{Z_1}^T;\mathbf{Z_2}^T;\mathbf{Z_3}^T;\mathbf{Z_4}^T\}$ with dimensions $n \times m_2$) are shown in the supplementary materials (sup_Z_vector.txt). New vectors $\mathbf{Z_i}$, even though formed through linear combination of compositional vectors, are abstract mathematical constructs without a direct chemical or physical interpretation, because coefficients of $\mathbf{T}$ are not restricted to be positive only. The four new vectors explain 53.73%, 35.90%, 5.49% and 3.40%, respectively, of the total variance. The total variance represented is 98.52%, which indicates that the top four vectors are sufficient to represent majority of the data.

A linear regression is performed between the four principal components Z_1, Z_2, Z_3, Z_4 and the volume V, using Eq. 7:

$$V = \alpha_1 \cdot Z_1 + \alpha_2 \cdot Z_2 + \alpha_3 \cdot Z_3 + \alpha_4 \cdot Z_4 + \beta \tag{7}$$

The fitted coefficients are $\alpha_1 = -10.46$, $\alpha_2 = 10.60$, $\alpha_3 = -3.96$, $\alpha_4 = -2.45$ and $\beta = 440.95$. The mean square error of the fitting is 2.39 Å^6 and the maximum mismatch between the predicted and the actual value is 1.62%. Figure 5 shows the linear regression results between the four new vectors and the unit cell volume along with the fitting residual. Good agreement is achieved between the fitting results and the actual values.

Elements in the transform matrix $\mathbf{T}$ show the projection of the normalized vector in the old space ($\mathbf{X_i}$) on the vector in the new space ($\mathbf{Z_j}$). By analyzing $\mathbf{T}$, we can have a better idea of the meaning of the principal components. The first interesting observation regarding $\mathbf{T}$ is that the last two rows (the 14th and the 15th rows) always have opposite values. The value in the 14th row is the projection of *Si* (in

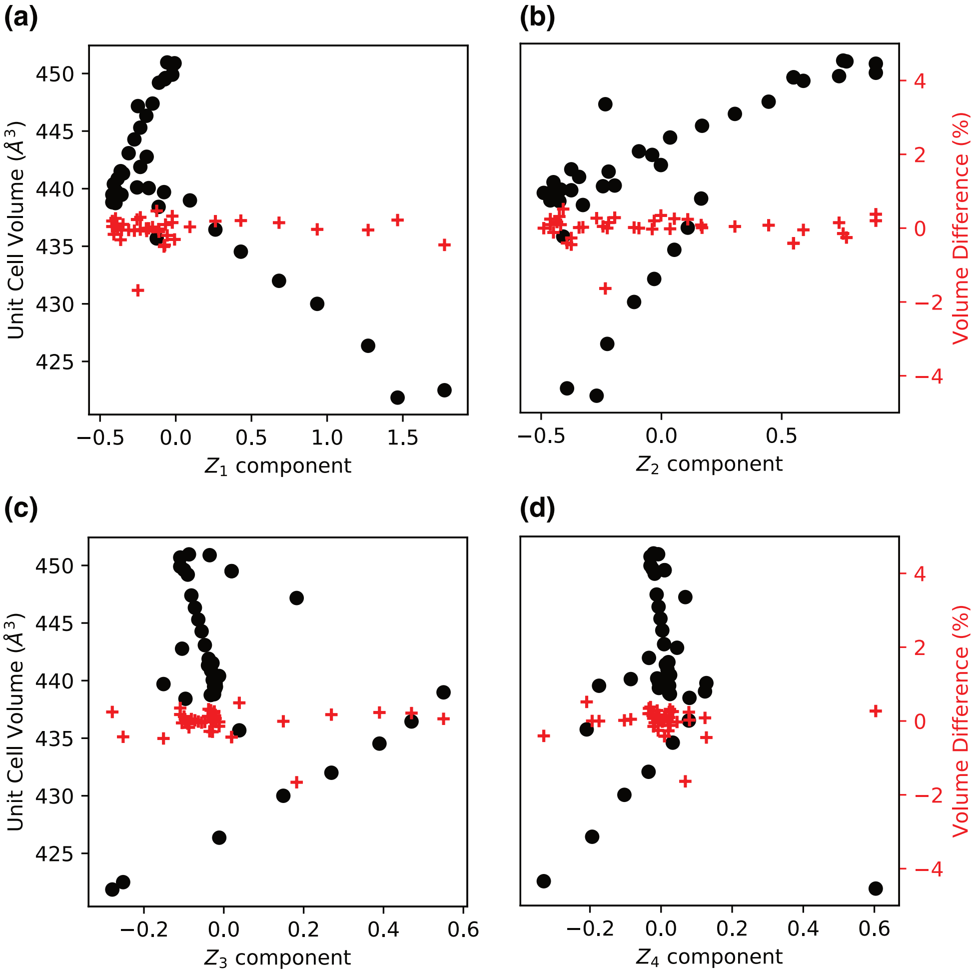

Fig. 5 Relationship between unit cell volumes and the four new principal vectors Z_i (i = 1, 2, 3, 4). Black dots represent the projection of unit cell volume to Z_i (i = 1, 2, 3, 4). Red crosses represent the residual from linear fitting

T site) to the new space and the value in the 15th row is the projection of Al (in T site) to the new space. Si (in T site) and Al (in T site) add up to a constant value and therefore have strong negative correlation. PCA correctly recognized the negative correlation between the two vectors and opposite numbers on the 14th and the 15th rows can maximize the variance. Therefore, the variance contribution of Si (in T site) and Al (in T site) can be combined and analyzed together. The elements in matrix $\mathbf{T}$ range from 10^{-1} to 10^{-4}. Therefore, the most important components in the old vectors are those with coefficients T_{ij} in the order of 10^{-1}. The first new vector, $\mathbf{Z_1}$, is the most important principal component which explains 53.73% of the total variance. Among the coefficients T_{i1} ($1<= i <=15$), $T_{9,1}$ and $T_{15,1}$ are in the order of 10^{-1} and have a positive sign. This means that contribution of the new vector $\mathbf{Z_1}$ increases as Al^{3+} (in M1 site) and Al (in T site) increase. Figure 5a shows the trend between $\mathbf{Z_1}$ and volume, there are roughly two branches, the branch, where volume decreases as $\mathbf{Z_1}$ component increases, is mainly caused by the increase in Al^{3+} in M1 site and Al in T site. $T_{6,1}$, which is the projection of normalized Mg^{2+} concentration in M1 site on $\mathbf{Z_1}$, is the element in T_{i1} which has the largest negative value. Therefore, the $\mathbf{Z_1}$ component decreases as Mg^{2+} in M1 site increases. The other branch in Fig. 5a shows negative correlation between volume and the concentration of Mg^{2+} in M1 site. Among the coefficients T_{i2} ($1<= i <=$ 15), $T_{7,2}$, which is the projection of Fe^{2+} in M1 site on $\mathbf{Z_2}$, has the largest positive value. In Fig. 5b, unit cell volume and the $\mathbf{Z_2}$ component are in general positively correlated. Therefore, unit cell volume and Fe^{2+} in M1 site have positive correlation.

Implications for the subducting slab

Diopside is the Mg-end member of omphacite—an important clinopyroxene in eclogite. It provides the pulling force for the subduction and is therefore relevant for the slab dynamics studies. The difference in chemistry of eclogitic diopside in various subduction zones has not been studied systematically, therefore, it is difficult to assess whether Fe-content differences in diopside from cold, and hot subducted slabs are the controlling factor of the slab pull, or a consequences of the different P–T-time paths of diopside residence in the slab. The densities of

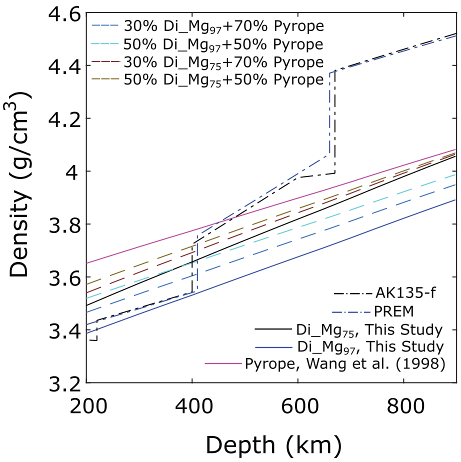

Fig. 6 Density of different mineral assemblages in the cold subducting slab

different diopside and pyrope samples (Hu et al. 2016) along the cold basalt geotherm (Ganguly et al. 2009) are shown in Fig. 6. The mineral assemblages with different diopside and pyrope proportions along with two seismic density profiles are also shown in Fig. 6. Along the cold basalt geotherm, at the base of the upper mantle, Di_Mg_{75} and pyrope are ∼3.5% and ∼6.9% denser than Di_Mg_{97}. A mineral assemblage of 30% Di_Mg_{75} + 70% pyrope is ∼2.4% denser than a mineral assemblage of 30% Di_Mg_{97} + 70% pyrope and is ∼4.2% denser than the density profile determined from seismic model AK135-f and PREM. A mineral assemblage of 50% Di_Mg_{75} + 50% pyrope is ∼1.7% denser than a mineral assemblage of 50% Di_Mg_{97} + 50% pyrope and is ∼4.9% denser than AK135-f and PREM model. Therefore, the cold basalt provides a pulling force to the slab in the upper mantle. Di_Mg_{75}, which has more Fe and Al, provides ∼2% more pulling force than the end-member diopside. Therefore, with more Fe^{2+} and Al^{3+}, the slab tends to have more pulling force.

At the base of the mantle transition zone, the diopside and pyrope mixtures are less dense than the density profile determined from seismology. The mineral assemblage of 30% Di_Mg_{75} + 70% pyrope is 2.6% denser than the mineral assemblage with 30% Di_Mg_{97} + 70% pyrope. This assemblage is 3.35% lighter than the seismic models. The mineral assemblage of 50% Di_Mg_{75} + 50% pyrope is 1.9% denser than the mineral assemblage with 50% Di_Mg_{97} + 50% pyrope. This assemblage is 3.0% lighter than the seismic models. At the top of the lower mantle, the 30% Di_Mg_{75} + 70% pyrope assemblage and the 50% Di_Mg_{75} + 50% pyrope assemblage are 10.5% and 10.3% lighter than the seismic models. Therefore, even with Di_Mg_{75}, which has more Fe and Al, the cold basalt is less dense than the surrounding mantle transition zone materials. This mineral assemblage still provides a buoyancy force to the slab, and could contribute to the slab stagnation observed at the bottom of the transition zone or the top of the lower mantle.

Conclusions

Diopside ($CaMgSi_2O_6$) is an important mineral in the subducted lithospheric plate. It is believed to dissolve into garnet at high-pressure and high-temperature conditions equivalent to the Earth's upper mantle. However, recent studies show that this reaction is kinetically inhibited at the conditions of cold subducting slab, and therefore clinopyroxene can be preserved down to the transition zone or even the top of the lower mantle (Faccenda and Dal Zilio 2017; Nishi et al. 2011; Van Mierlo et al. 2013). We reported the results of high-pressure single-crystal X-ray diffraction experiments conducted on aluminous iron-bearing diopside and a nearly end-member diopside up to 50 GPa in diamond anvil cell. The density functional theory calculations of end-member diopside are also reported. The bulk modulus and its pressure derivative are determined to be 123(3) GPa and 4.5(3) for the nearly end-member diopside and 113(1) GPa and 4.46(9) for the aluminous iron-bearing diopside. These results are compared with hedenbergite ($CaFeSi_2O_6$) and Ca–Tschermak ($CaAlAlSiO_6$), and indicate that Fe in clinopyroxene structure increases bulk modulus and Al decreases bulk modulus. The structure of diopside is compared with hedenbergite and $Di_{80}En_{20}$. Diopside has shorter a axis than hedenbergite and this is caused by the smaller cation size of Mg^{2+}, compared to Fe^{2+}. The β angle of Mg-rich clinopyroxene such as diopside and $Di_{80}En_{20}$ show a flattening at ∼30 GPa. The effect of Fe^{2+} and Al^{3+} in the unit cell volume of Mg-, Fe- and Al-rich clinopyroxenes are analyzed using principal component analysis. Positive correlation is observed between Al and unit cell volume and negative correlation is shown between Fe and unit cell volume. The densities of the two diopside samples are modeled along the cold subducting slab geotherm (Ganguly et al. 2009) and are compared with the seismic models. Aluminous iron-bearing diopside shows higher density than the end-member diopside. Therefore, in the upper mantle, aluminous iron-bearing diopside provides stronger pulling force to the subducted slab. At the bottom of the transition zone and top of the lower mantle, eclogite with aluminous iron-bearing diopside has higher density than that with end-member diopside. However, it is still less dense than the surrounding mantle and therefore could contribute to the buoyancy force, which explains the slab stagnation phenomena observed at that depth.

Acknowledgements The project was supported by the National Science Foundation Division of Earth Sciences Geophysics grant 1722969 to P.D. Development of the ATREX software, used for experimental data analysis was supported by NSF EAR GeoInformatics grant 1440005. JSZ is supported by the National Science Foundation (NSF) under Grant EAR 1646527 (JSZ) and the start-up fund from UNM (JSZ). The experimental part of this work was performed at GeoSoilEnviroCARS (Sector 13), Advanced Photon Source (APS), Argonne National Laboratory. GeoSoilEnviroCARS is supported by the National Science Foundation-Earth Sciences (EAR-1128799) and Department of Energy-Geosciences (DE-FG02-94ER14466). Use of the COMPRES-GSECARS gas loading system was supported by COMPRES under NSF Cooperative Agreement EAR-1661511. Use of the Advanced Photon Source was supported by the US Department of Energy, Office of Science, Office of Basic Energy Sciences, under Contract No. DE-AC02-06CH11357. We would also like to thank Carnegie-DOE Alliance Center for support through Academic Partner subcontract to P.D. and Prof. T.S.Duffy at Princeton University for kindly providing the single crystal samples from the Harry Hess collection. B.K. would like to acknowledge computational resources that were made available by the National Science Foundation through XSEDE under grant number DMR TG-110093.

References

Akaogi M, Yano M, Tejima Y, Iijima M, Kojitani H (2004) High-pressure transitions of diopside and wollastonite: phase equilibria and thermochemistry of $CaMgSi_2O_6$, $CaSiO_3$ and $CaSi_2O_5$-$CaTiSiO_5$ system. Phys Earth Planet Inter 143–144:145–156

Anderson DL, Bass JD (1984) Mineralogy and composition of the upper mantle. Geophys Res Lett 11(7):637–640

Asahara Y, Ohtani E, Kondo T, Kubo T, Miyajima N, Nagase T, Fujino K, Yagi T, Kikegawa T (2005) Formation of metastable cubic-perovskite in high-pressure phase transformation of ca (mg, fe, al) Ca(Mg, Fe, Al)Si_2O_6. Am Mineral 90(2–3):457–462

Bass JD, Anderson DL (1984) Composition of the upper mantle: geophysical tests of two petrological models. Geophys Res Lett 11(3):229–232

Blöchl PE (1994) Projector augmented-wave method. Phys Rev B 50(24):17953

Cameron M, Papike J (1981) Structural and chemical variations in pyroxenes. Am Mineral 66(1–2):1–50

Canil D (1994) Stability of clinopyroxene at pressure-temperature conditions of the transition region. Phys Earth Planet Inter 86(1):25–34

Dera P, Finkelstein G, Duffy T, Downs R, Meng Y, Prakapenka V, Tkachev S (2013a) Metastable high-pressure transformations of orthoferrosilite Fs_{82}. Phys Earth Planet Inter 221:15–21

Dera P, Zhuravlev K, Prakapenka V, Rivers M, Finkelstein G, Grubor-Urosevic O, Tschauner O, Clark S, Downs R (2013b) High pressure single-crystal micro X-ray diffraction analysis with GSE_ADA/RSV software. High Press Res 33(3):466–484

Dewaele A, Datchi F, Loubeyre P, Mezouar M (2008) High pressure-high temperature equations of state of neon and diamond. Phys Rev B 77(9):094106

Faccenda M, Dal Zilio L (2017) The role of solid-solid phase transitions in mantle convection. Lithos 268:198–224

Flemming RL, Terskikh V, Ye E (2015) Aluminum environments in synthetic Ca-tschermak clinopyroxene ($CaAlAlSiO_6$) from rietveld refinement, ^{27}Al NMR, and first-principles calculations. Am Mineral 100(10):2219–2230

Frost DJ (2008) The upper mantle and transition zone. Elements 4(3):171–176

Fukao Y, Obayashi M (2013) Subducted slabs stagnant above, penetrating through, and trapped below the 660 km discontinuity. J Geophys Res 118(11):5920–5938

Fukao Y, Obayashi M, Nakakuki T, Group DSP (2009) Stagnant slab: a review. Ann Rev Earth Planet Sci 37:19–46

Ganguly J, Freed AM, Saxena SK (2009) Density profiles of oceanic slabs and surrounding mantle: Integrated thermodynamic and thermal modeling, and implications for the fate of slabs at the 660 km discontinuity. Phys Earth Planet Inter 172(3):257–267

Green E, Holland T, Powell R (2007) An order-disorder model for omphacitic pyroxenes in the system jadeite-diopside-hedenbergite-acmite, with applications to eclogitic rocks. Am Mineral 92(7):1181–1189

Grossman L, Larimer JW (1974) Early chemical history of the solar system. Rev Geophys 12(1):71–101

Hazen RM, Downs RT (2000) High-temperature and high-pressure crystal chemistry, Reviews in mineralogy and geochemistry, vol 41. Mineralogical Society of America, Blacksburg

Hu Y, Dera P, Zhuravlev K (2015) Single-crystal diffraction and Raman spectroscopy of hedenbergite up to 33 GPa. Phys Chem Miner 42(7):595–608

Hu Y, Kiefer B, Bina CR, Zhang D, Dera PK (2017) High-pressure γ-$CaMgSi_2O_6$: Does penta-coordinated silicon exist in the earth's mantle? Geophys Res Lett 44(22):11–340

Hu Y, Wu Z, Dera PK, Bina CR (2016) Thermodynamic and elastic properties of pyrope at high pressure and high temperature by first-principles calculations. J Geophys Res 121(9):6462–6476

Irifune T, Miyashita M, Inoue T, Ando J, Funakoshi K, Utsumi W (2000) High-pressure phase transformation in $CaMgSi_2O_6$ and implications for origin of ultra-deep diamond inclusions. Geophys Res Lett 27(21):3541–3544

Ita J, Stixrude L (1992) Petrology, elasticity, and composition of the mantle transition zone. J Geophys Res 97(B5):6849–6866

James G, Witten D, Hastie T, Tibshirani R (2013) An introduction to statistical learning, vol 112. Springer, Berlin

Kandelin J, Weidner DJ (1988) Elastic properties of hedenbergite. J Geophys Res 93(B2):1063–1072

Kim Y-H, Ming LC, Manghnani MH (1994) High-pressure phase transformations in a natural crystalline diopside and a synthetic $CaMgSi_2O_6$ glass. Phys Earth Planet Inter 83(1):67–79

King S, Frost D, Rubie D (2015) Why cold slabs stagnate in the transition zone. Geology 43(3):231–234

Kresse G, Furthmüller J (1996a) Efficiency of ab-initio total energy calculations for metals and semiconductors using a plane-wave basis set. Comput Mater Sci 6(1):15–50

Kresse G, Furthmüller J (1996b) Efficient iterative schemes for ab initio total-energy calculations using a plane-wave basis set. Phys Rev B 54(16):11169

Li B, Neuville D (2010) Elasticity of diopside to 8 GPa and 1073 K and implications for the upper mantle. Phys Earth Planet Inter 183(34):398–403

Liu L-G (1979) The system enstatite-wollastonite at high pressures and temperatures, with emphasis on diopside. Phys Earth Planet Inter 19(3):P15–P18

Mao H, Xu J, Bell P (1986) Calibration of the ruby pressure gauge to 800 kbar under quasi-hydrostatic conditions. J Geophys Res 91(B5):4673–4676

Momma K, Izumi F (2011) Vesta 3 for three-dimensional visualization of crystal, volumetric and morphology data. J Appl Crystallogr 44(6):1272–1276

Nishi M, Kato T, Kubo T, Kikegawa T (2008) Survival of pyropic garnet in subducting plates. Phys Earth Planet Inter 170(3–4):274–280

Nishi M, Kubo T, Kato T, Tominaga A, Funakoshi K-I, Higo Y (2011) Exsolution kinetics of majoritic garnet from clinopyroxene in subducting oceanic crust. Phys Earth Planet Inter 189(1):47–55

Nishi M, Kubo T, Ohfuji H, Kato T, Nishihara Y, Irifune T (2013) Slow Si-Al interdiffusion in garnet and stagnation of subducting slabs. Earth Planet Sci Lett 361:44–49

Oguri K, Funamori N, Sakai F, Kondo T, Uchida T, Yagi T (1997) High-pressure and high-temperature phase relations in diopside $CaMgSi_2O_6$. Phys Earth Planet Inter 104:363–370

Pedregosa F, Varoquaux G, Gramfort A, Michel V, Thirion B, Grisel O, Blondel M, Prettenhofer P, Weiss R, Dubourg V, Vanderplas J, Passos A, Cournapeau D, Brucher M, Perrot M, Duchesnay E (2011) Scikit-learn: machine learning in python. J Mach Learn Res 12:2825–2830

Perdew JP, Zunger A (1981) Self-interaction correction to density-functional approximations for many-electron systems. Phys Rev B 23(10):5048

Plank T, Langmuir CH (1998) The chemical composition of subducting sediment and its consequences for the crust and mantle. Chem Geol 145(3):325–394

Plonka A, Dera P, Irmen P, Rivers M, Ehm L, Parise J (2012) β-diopside, a new ultrahigh-pressure polymorph of $CaMgSi_2O_6$ with six-coordinated silicon. Geophys Res Lett 39(24)

Poli S (1993) The amphibolite-eclogite transformation; an experimental study on basalt. Am J Sci 293(10):1061–1107

Poli S, Schmidt MW (2002) Petrology of subducted slabs. Ann Rev Earth Planet Sci 30(1):207–235

Rigden SM, Ahrens TJ, Stolper E (1989) High-pressure equation of state of molten anorthite and diopside. J Geophys Res 94(B7):9508–9522

Ringwood A (1967) The pyroxene-garnet transformation in the earth's mantle. Earth Planet Sci Lett 2(3):255–263

Ringwood AE (1975) Composition and petrology of the earth's mantle. MacGraw-Hill, New York, p 618

Ringwood AE (1982) Phase transformations and differentiation in subducted lithosphere: implications for mantle dynamics, basalt petrogenesis, and crustal evolution. J Geol 90(6):611–643

Rivers M, Prakapenka VB, Kubo A, Pullins C, Holl CM, Jacobsen SD (2008) The COMPRES/GSECARS gas-loading system for diamond anvil cells at the advanced photon source. High Press Res 28(3):273–292

Rubin AE (1997) Mineralogy of meteorite groups. Meteorit Planet Sci 32(2):231–247

Sang L, Bass JD (2014) Single-crystal elasticity of diopside to 14 GPa by Brillouin scattering. Phys Earth Planet Inter 228:75–79

Sheldrick G (2008) A short history of shelx. Acta Crystallogr Sect A 64(1):112–122

Subramanian A (1962) Pyroxenes and garnets from charnockites and associated granulites. Bulletin of the Geological Society of America 21–36

Svendsen B, Ahrens TJ (1983) Dynamic compression of diopside and salite to 200 GPa. Geophys Res Lett 10(7):501–504

Svendsen B, Ahrens TJ (1990) Shock-induced temperatures of $CaMgSi_2O_6$. J Geophys Res 95(B5):6943–6953

Thompson R, Downs R (2008) The crystal structure of diopside at pressure to 10 GPa. Am Mineral 93:177–186

Tomioka N, Kimura M (2003) The breakdown of diopside to Ca-rich majorite and glass in a shocked H chondrite. Earth Planet Sci Lett 208(3–4):271–278

Van Mierlo W, Langenhorst F, Frost D, Rubie D (2013) Stagnation of subducting slabs in the transition zone due to slow diffusion in majoritic garnet. Nat Geosci 6(5):400

Walker AM (2012) The effect of pressure on the elastic properties and seismic anisotropy of diopside and jadeite from atomic scale simulation. Phys Earth Planet Inter 192:81–89

Walker AM, Tyer RP, Bruin RP, Dove MT (2008) The compressibility and high pressure structure of diopside from first principles simulation. Phys Chem Miner 35(7):359–366

Zhang A, Hsu W, Wang R, Ding M (2006) Pyroxene polymorphs in melt veins of the heavily shocked Sixiangkou L6 chondrite. Euro J Mineral 18(6):719–726

Zhang L, Ahsbahs H, Hafner SS, Kutoglu A (1997) Single-crystal compression and crystal structure of clinopyroxene up to 10 GPa. Am Mineral 82:245–258

Zhao Y (1998) Thermoelastic equation of state of monoclinic pyroxene: $CaMgSi_2O_6$ diopside. Rev High Press Sci Technol 7:25–27